Chinese Chemical Letters 37 (2026) 112353

Contents lists available at ScienceDirect

Chinese Chemical Letters

journal homepage: www.elsevier.com/locate/cclet

Sustainable molecular oxygen activation for efficient treatment of heavy-metal complexes by fissured-phosphorylated zero-valent iron

Yuhang Zhang[a], Haiming Cai[a], Chuling Guo[a], Guining Lu[a], Zhi Dang[a,*], Xiao Liu[b], Falong Jia[b,*], Zhihui Ai[b], Chunhua Feng[a]

[a] The Key Lab of Pollution Control and Ecosystem Restoration in Industry Clusters, Ministry of Education, South China University of Technology, Guangzhou 510006, China
[b] College of Chemistry, Central China Normal University, Wuhan 430079, China

ARTICLE INFO

Article history:
Received 30 September 2025
Revised 12 December 2025
Accepted 30 December 2025
Available online 31 December 2025

Keywords:
Sustainable molecular oxygen activation
Heavy-metal complexes degradation
Metal recovery
Fissured-phosphorylated zero-valent iron
Ferrous cycle regeneration

ABSTRACT

Heavy metals complexed with organic reagents in wastewater jeopardize environmental safety, resist conventional removal methods, but are also valuable metallic resources. Herein, a novel fissured-phosphorylated zero-valent iron (P-ZVI$^{bm\&ln}$) was synthesized *via* mechanochemical phosphorylation and liquid-nitrogen-quenching, and applied to benzohydroxamic acid-complexed Cu(II) (Cu(II)-BHA) degradation and synchronous copper recovery. During mechanochemical phosphorylation, a ferrous phosphate shell with abundant surface ferrous ($\equiv Fe^{2+}$) was constructed on ZVI, which facilitated the activation of molecular oxygen into reactive oxygen species (ROS) for Cu(II)-BHA degradation. Moreover, the subsequent liquid-nitrogen-quenching created surface cracks for more Fe^0 cores exposure, which triggered the comproportionation reaction ($Fe^0 + 2Fe^{3+} \rightarrow 3Fe^{2+}$), thereby strengthening Fe^{2+} regeneration and sustainable molecular oxygen activation for efficient oxidative decomplexation and metal recovery. In the P-ZVI$^{bm\&ln}$/Cu(II)-BHA decontamination process, nearly 100 % of Cu was recovered and BHA was degraded, while P-ZVI$^{bm\&ln}$ showed excellent cyclic reaction performance. Through diverse experiments and density functional theory (DFT) calculations, researchers shed light on the mechanism. Meanwhile, the P-ZVI$^{bm\&ln}$ could effectively treat other metal-BHA complexes (*e.g.*, Cr(III), Mn(II), Ni(II), Ag(I), Cd(II), and Pb(II)) and actual mine wastewater containing Cu(II) complexes with satisfactory metal recovery, showing promising application prospects in treatment of heavy-metal complex wastewater and sustainable development.

© 2026 Published by Elsevier B.V. on behalf of Chinese Chemical Society and Institute of Materia Medica, Chinese Academy of Medical Sciences.

Heavy-metal ions form stable and mobile complexes with organic reagents in mine wastewater, worsening toxicity and hampering heavy-metal recovery [1]. In sustainable terms, treating heavy-metal complex pollution demands simultaneous heavy-metal resource reclamation and organic-ligands degradation [2]. Modifying ZVI is a leading method for removing heavy metals and organic-ligands from wastewater. A probable focus of ZVI modification is boosting $\equiv Fe^{2+}$, which can activate molecular oxygen, a green oxidant, to generate reactive oxygen species (ROS) for oxidizing organic-ligands, thus slashing costs without additional oxidants [3]. The extraction of heavy-metal ions by ZVI relies on reduction by Fe^0 [4]. Hence, ZVI modification should not only increase the $\equiv Fe^{2+}$ but also improve internal Fe^0 accessibility.

Herein, industrial micro-ZVI was first ball-milled with tiny sodium dihydrogen phosphate to form phosphorylated micro-ZVI (P-ZVI^{bm}), which then underwent liquid-nitrogen-quenching to produce P-ZVI$^{bm\&ln}$. Subsequently, the P-ZVI$^{bm\&ln}$ was deployed for decontaminating paradigmatic heavy metal-beneficiation reagent complex, Cu(II)-BHA. The physicochemical properties of P-ZVI$^{bm\&ln}$ were characterized using atomic force microscope (AFM), Mössbauer spectrum, and ToF-SIMS, *etc*. The ferrous phosphate shell enriched $\equiv Fe^{2+}$ sites in P-ZVI$^{bm\&ln}$ to activate dissolved oxygen to ROS. In Cu(II)-BHA decontamination, ROS oxidatively decomplexed Cu(II)-BHA, releasing Cu^{2+} and degrading BHA. The released Cu^{2+} was synchronously recovered by P-ZVI$^{bm\&ln}$, mainly reduced and immobilized, with minor precipitation by PO_4^{3-}. Phosphorylation markedly improved the performance of P-ZVI$^{bm\&ln}$ in BHA degradation, increasing the rate constant by nearly 200-fold. Moreover, the liquid-nitrogen-quenching prominently reinforced continuous Cu(II) extraction (recovery ratio >97.7 %) and cyclic reactivity during Cu(II)-BHA degradation. The removal, recovery mechanisms, and performance reinforcement were thoroughly elucidated *via* electron paramagnetic resonance (EPR), high resolution X-ray

* Corresponding authors.
E-mail addresses: chzdang@scut.edu.cn (Z. Dang), fljia@ccnu.edu.cn (F. Jia).

https://doi.org/10.1016/j.cclet.2025.112353
1001-8417/© 2026 Published by Elsevier B.V. on behalf of Chinese Chemical Society and Institute of Materia Medica, Chinese Academy of Medical Sciences.

photoelectron spectroscopy (HR-XPS), *in-situ* Raman, and *in-situ* attenuated total internal reflectance Fourier transform infrared spectroscopy (ATR-FTIR), *etc*., and supported by density functional theory (DFT) calculations (including charge density difference, density of states, and frontier orbitals).

Ferrous regeneration is crucial for overcoming the cyclic limitations of Fenton-like reactions, but most catalyst-assisted methods are intricate [5,6]. This study pioneered a simple liquid-nitrogen-quenching for the physical remodeling of surface morphology, conspicuously advancing ferrous regeneration for the first time. Impressively, liquid-nitrogen-quenching of P-ZVI$^{bm\&ln}$ induced cracks, exposing more Fe^0 cores, which prominently boosted heavy-metal recovery and actuated ferrous regeneration *via* comproportionation ($Fe^0 + 2Fe^{3+} \rightarrow 3Fe^{2+}$). This efficient iron-cycling synergism vigorously overcame the ferrous regeneration bottleneck, driving sustainable molecular oxygen activation to ROS while substantially enhancing cyclic degradation and reclamation capacity. In practice, P-ZVI$^{bm\&ln}$ treated actual mine wastewater containing beneficiation reagents and heavy-metals effectively, satisfactorily mineralized organic reagents, while recovering heavy metals without additional precipitants in a one-stop treatment. The treated effluent met discharge standards for chemical oxygen demand (COD) and heavy metals, underscoring its recyclability and extensive application potential.

Synthesis strategy of P-ZVI$^{bm\&ln}$ was illustrated in Fig. S1 (Supporting information). AFM analysis indicated phosphorylation roughened P-ZVI^{bm}, and liquid-nitrogen-quenching induced surface cracks in P-ZVI$^{bm\&ln}$ (Figs. 1a-c). HR-XPS (Fe 2p) analysis (Figs. 1d-f) revealed phosphorylation elevated surface ferrous ($\equiv Fe^{2+}$) content from 30.6 % (ZVI^{bm}) to 52.8 % (P-ZVI^{bm}), possibly enhancing catalytic activation of dissolved molecular oxygen [7,8]. Liquid-nitrogen-quenching boosted surface Fe^0 from 14.8 % (P-ZVI^{bm}) to 30.0 % (P-ZVI$^{bm\&ln}$), potentially aiding heavy-metal ions reduction for recovery [9]. SEM-mapping, HR-XPS, and FTIR analysis clarified that phosphorylation incorporated phosphate into ZVI; whereas the liquid-nitrogen-quenching did not introduce N (Figs. S2-S4 in Supporting information). Therefore, cracking resulting from liquid-nitrogen-quenching was attributed to the extreme temperature gradient, excluding any nitrogen doping or chemical reactions. The TGA and DTG of P-ZVI$^{bm\&ln}$ and ferrous phosphate demonstrated that their thermal decomposition profiles closely matched, suggesting P-ZVI$^{bm\&ln}$ presumably contained ferrous phosphate (Fig. S5 in Supporting information). The Mössbauer spectrum of ZVI$^{bm\&ln}$ was fitted to three spectral components corresponding to elemental iron (89.7 %), ferric oxyhydroxide (7.9 %), and ferrous oxide (2.4 %) (Fig. S6 and Table S1 in Supporting information). For P-ZVI$^{bm\&ln}$, the Mössbauer spectrum was also fitted to three iron-containing components, which were identified as elemental iron (90.7 %), ferrous phosphate (6.6 %), and ferric phosphate (2.7 %), authenticating ferrous phosphate formation (Fig. 1g and Table S2 in Supporting information) [10,11]. The selected area electron diffraction (SAED) pattern of P-ZVI$^{bm\&ln}$ displayed diffraction spots for iron planes (200), (001), (211), and ferrous phosphate planes (310), (001), indicating ferrous phosphate formation (Fig. 1h) [12]. TEM-mapping and energy dispersive spectroscopy (EDS) further revealed a phosphorus-rich shell approximately 50-100 nm thick (Fig. S7 in Supporting information) [13]. ToF-SIMS analysis of P-ZVI$^{bm\&ln}$ identified iron and ferrous phosphate, with a 3D depth profile confirming a ~50 nm thick ferrous phosphate shell (Fig. 1i and Fig. S8 in Supporting information) [14]. SEM results revealed liquid-nitrogen-quenching cracked P-ZVI$^{bm\&ln}$ surface, forming fissures (Fig. S9 in Supporting information). AFM and potential analysis of P-ZVI$^{bm\&ln}$ following liquid-nitrogen-quenching revealed cracks of 173-463 nm width and 72-81 nm depth, potentially exposing more Fe^0. Lower potential at crack bottoms than surfaces in potential analysis indicated enhanced electron migration from interior to surface (Fig. S10 in Supporting information). Minor reductions in particle size and slight increases in specific surface area were observed in ZVI following phosphatation and liquid-nitrogen-quenching (Fig. S11 in Supporting information).

The UV-vis spectral blue shift and alkali precipitation experiment verified the Cu(II)-BHA complex formation (Fig. S12 and Text S5 in Supporting information). Reliable and comprehensive detection methods for Cu(II)-BHA were presented in Figs. S13 and S14 (Supporting information). P-ZVI$^{bm\&ln}$ with 7 % molar-ratio (n_P:n_{ZVI} = 7 %) showed optimal TOC (total organic carbon) and total Cu removal in treatment of Cu(II)-BHA, and this sample was investigated in further studies (Fig. S15 and Text S6 in Supporting information). ZVI^{bm} and ZVI$^{bm\&ln}$ exhibited negligible efficacy in removing BHA from Cu(II)-BHA (Fig. 2a). In comparison, P-ZVI^{bm} removed approximately 92.1 % of BHA and 90.0 % of total Cu, while P-ZVI$^{bm\&ln}$ removed nearly 100 % of both BHA and total Cu (Figs. 2a and b). Compared to ZVI$^{bm\&ln}$, P-ZVI$^{bm\&ln}$ markedly improved the reaction rate constants for BHA and total Cu removal by approximately 200-fold and 3.4-fold, respectively (Fig. S16 in Supporting information). The specific surface area-normalized reaction rate constants also remained significantly enhanced. TOC analysis results displayed TOC changed little in the presence of ZVI^{bm} and ZVI$^{bm\&ln}$, while P-ZVI^{bm} and P-ZVI$^{bm\&ln}$ greatly decreased TOC by 79.5 % and 85.3 % respectively (Fig. 2c). In continuous cyclic treatment of Cu(II)-BHA, P-ZVI$^{bm\&ln}$ exhibited superior removal capabilities and could remove 93.0 % of BHA after the 6th cycle. In sharp contrast, P-ZVI^{bm} only removed 12.1 % of BHA, while ZVI^{bm} and ZVI$^{bm\&ln}$ barely removed BHA. Meanwhile, P-ZVI$^{bm\&ln}$ maintained removal ratio above 90.5 % of total Cu in six cycles (Figs. 2d and e), greatly surpassing the performance of other samples. In addition, P-ZVI$^{bm\&ln}$ could work well in wide pH range and in the presence of coexisting ion during Cu(II)-BHA decontamination (Fig. S17 in Supporting information). Besides BHA, other beneficiation reagents (diethyldithiocarbamate (DDTC), ethylxanthate (EX)) and coal-mine-wastewater pollutant (phenol) could be efficiently degraded by P-ZVI$^{bm\&ln}$ (Fig. 2f), demonstrating the universality of P-ZVI$^{bm\&ln}$ in organic-pollutant degradation. SEM-mapping of reacted P-ZVI$^{bm\&ln}$ showed obvious copper signals, demonstrating the extraction copper from wastewater (Fig. 2g). Recovery tests revealed that in six cycles, P-ZVI$^{bm\&ln}$ achieved copper recovery ratio of approximately 99.9 %, 99.9 %, 99.4 %, 97.7 %, 96.2 %, and 90.5 % from Cu(II)-BHA, highlighting its advantages in wastewater treatment and heavy-metal resource reclamation (Fig. 2h). To explore versatility, we used P-ZVI$^{bm\&ln}$ to treat BHA complexes of Cr(III), Mn(II), Ni(II), Ag(I), Cd(II) and Pb(II). Results showed P-ZVI$^{bm\&ln}$ degraded over 95 % of the BHA ligand and recovered multiple heavy metals efficiently (recovery ratio: approximately Cr 80.4 %, Mn 96.1 %, Ni 94.4 %, Ag nearly 100 %, Cd 81.8 %, Pb 99.4 %), indicating its powerful ligand-degradation and metal-recovery capabilities (Fig. 2i). In summary, mechanochemical phosphorylation and liquid-nitrogen-quenching of ZVI greatly improved its performance towards organic-ligands removal and metallic resource recovery, elevating its persistent cyclic decontamination prowess for heavy-metal complexes.

Further experiments under different atmospheres indicated that the dissolved oxygen played an important role in the removal of BHA ligand (Fig. S18 in Supporting information). Desorption tests showed that only 0.8 % Cu(II)-BHA was removed by adsorption (Fig. S19 in Supporting information), indicating most of the organic-ligands were removed by degradation [15–17]. ROS quenching experiments showed the dominant ROS within P-ZVI$^{bm\&ln}$ system were $O_2^{\bullet-}$, $^{\bullet}OH$, and $^1O_2$ (Fig. S20 in Supporting information) [18,19]. EPR analysis identified $O_2^{\bullet-}$, $^{\bullet}OH$, and $^1O_2$ through DMPO-$O_2^{\bullet-}$, DMPO-$^{\bullet}OH$, and TEMP-$^1O_2$ signals in P-ZVI$^{bm\&ln}$ system (Fig. 3a) [7,20]. Degradation experiments in D_2O demonstrated that P-ZVI$^{bm\&ln}$ significantly enhanced the performance in BHA

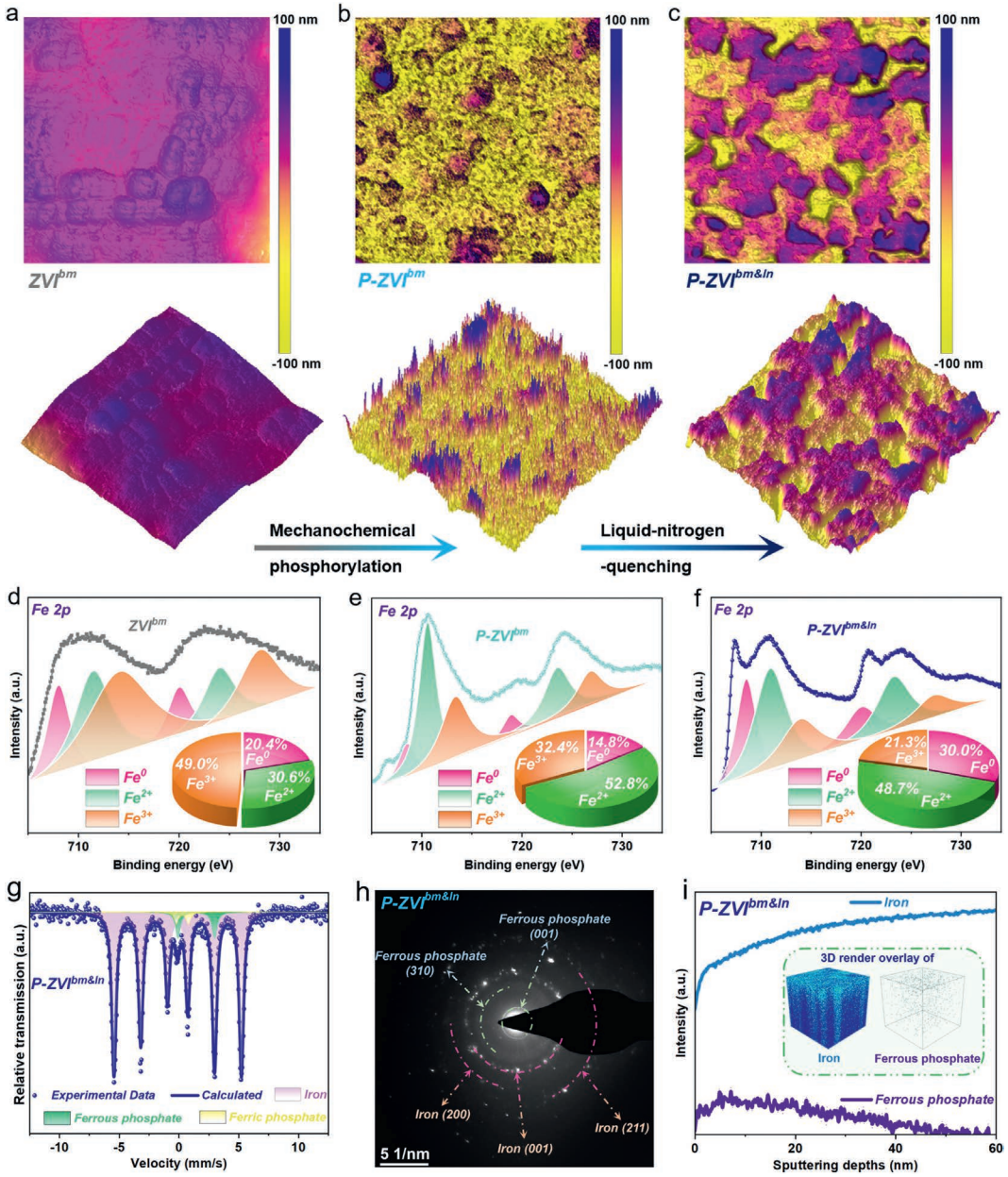


Fig. 1. The AFM results of ZVI$^{bm\&ln}$ (a), P-ZVI^{bm} (b), and P-ZVI$^{bm\&ln}$ (c). HR-XPS (Fe 2p) spectra of ZVI^{bm} (d), P-ZVI^{bm} (e), and P-ZVI$^{bm\&ln}$ (f). Mössbauer spectra (g), SAED (h), ToF-SIMS with 3D distribution (i) analysis of P-ZVI$^{bm\&ln}$.

removal, affirming contribution of $^1O_2$ to degradation (Fig. S21 in Supporting information) [21,22]. Quantitative ROS results revealed an $O_2^{\bullet-}$ yield of approximately 10.0 mmol/L, which dropped to 0.9 mmol/L with Fe^{2+}-chelator *o*-Phen, emphasizing the critical role of ferrous in molecular oxygen inhibited by *o*-Phen, confirming essential role of Fe^{2+} [23]. Moreover, the P-ZVI$^{bm\&ln}$ system generated far more $^{\bullet}OH$ and $^1O_2$ than ZVI$^{bm\&ln}$ (Fig. S22 in Supporting information). Results verified that P-ZVI$^{bm\&ln}$ activated molecular oxygen *via* Fe^{2+}-driven two-step, one-electron reduction ($O_2 + Fe^{2+} \rightarrow O_2^{\bullet-} + Fe^{3+}$, $O_2^{\bullet-} + Fe^{2+} + 2H^+ \rightarrow H_2O_2 + Fe^{3+}$). $O_2^{\bullet-}$ reacted with H_2O_2 to generate $^{\bullet}OH$ and $^1O_2$ through the Haber-Weiss reaction ($O_2^{\bullet-} + H_2O_2 \rightarrow {}^{\bullet}OH + {}^1O_2 + OH^-$). $O_2^{\bullet-}$ was converted to $^1O_2$ *via* disproportionation ($2O_2^{\bullet-} + 2H^+ \rightarrow H_2O_2 + {}^1O_2$) or oxidation by $^{\bullet}OH$ ($O_2^{\bullet-} + {}^{\bullet}OH \rightarrow {}^1O_2 + OH^-$) [24].

Given log*K*[Cu(II)-BHA] < log*K*[Fe(III)-BHA], leached Fe^{3+} in both systems could decomplex Cu(II)-BHA *via* replacement (Fig. S23 in Supporting information) [24]. Argon atmosphere hindered Fe^{3+} leaching, suppressing decomplexation and Cu removal (Fig. S24 in Supporting information), indicating minimal direct reduction of complexed-Cu(II) by Fe^0. Citrate (Fe^{3+} mask) markedly dropped Cu removal in ZVI$^{bm\&ln}$ (relying on Fe^{3+} replacement to liberate Cu^{2+} for reduction), but allowed 50.1 % removal in P-ZVI$^{bm\&ln}$ (both replacement and oxidative degradation acting). Ca^{2+} (PO_4^{3-} mask) slightly decreased Cu removal (~9.8 %), showing minor PO_4^{3-}-induced precipitation (Fig. S24). HR-XPS analysis of the reacted P-ZVI$^{bm\&ln}$ showed an obvious signal of Cu species in the state of primary Cu^0/Cu^I and minor Cu^{II} (Fig. S25 in Supporting information); Cu LMM analysis further revealed 56.9 % Cu^0, 14.7 % Cu^I, and 28.4 % Cu^{II}. Etching result revealed deeper regions with higher Cu^0, (75.3 %), indicating liquid-nitrogen-quenching-induced cracks exposed more Fe^0, enhancing Cu(II) reduction/reclamation (Fig. 3b). *In-situ* Raman showed P-ZVI$^{bm\&ln}$ contained 71.4 % ferrous phosphate and 28.6 % ferric phosphate (Fig. 3c and Fig. S26 in Supporting information). After Cu(II)-BHA addition, corrosion prod-

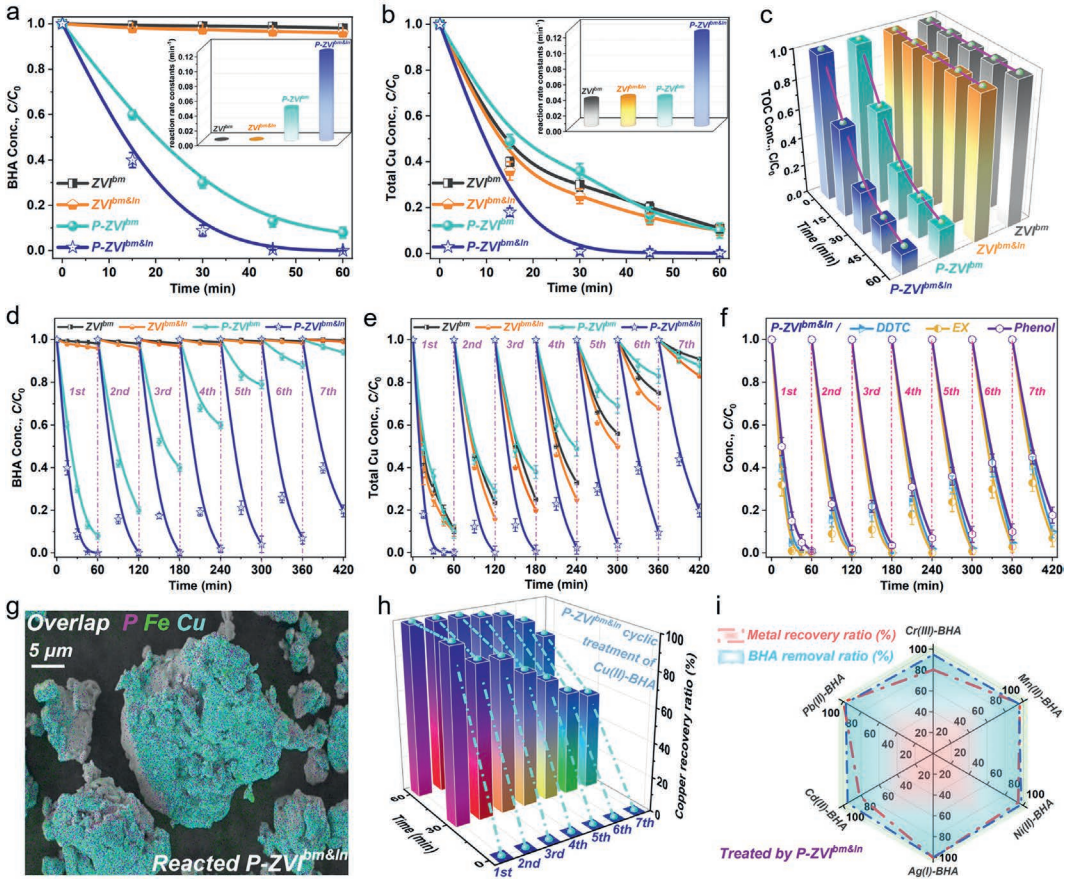


Fig. 2. Performance of ZVI^{bm}, ZVI$^{bm\&ln}$, P-ZVI^{bm}, and P-ZVI$^{bm\&ln}$ in removing BHA (a), total Cu (b) and TOC (c) from Cu(II)-BHA (0.2 mmol/L, 100 mL); the illustration depicts the reaction rate constant. BHA (d) and total Cu (e) cyclic removal efficiency by ZVI^{bm}, ZVI$^{bm\&ln}$, P-ZVI^{bm}, and P-ZVI$^{bm\&ln}$ from Cu(II)-BHA. (f) Cyclic removal performance of P-ZVI$^{bm\&ln}$ for DDTC, EX and phenol (0.2 mmol/L, 100 mL). SEM-mapping (g) of P-ZVI$^{bm\&ln}$ post Cu(II)–BHA removal and its copper recovery performance (h) in continuous decontamination. (i) Performance of P-ZVI$^{bm\&ln}$ in degrading other metal complexes (0.2 mmol/L, 100 mL) and metallic resource recovery ratio.

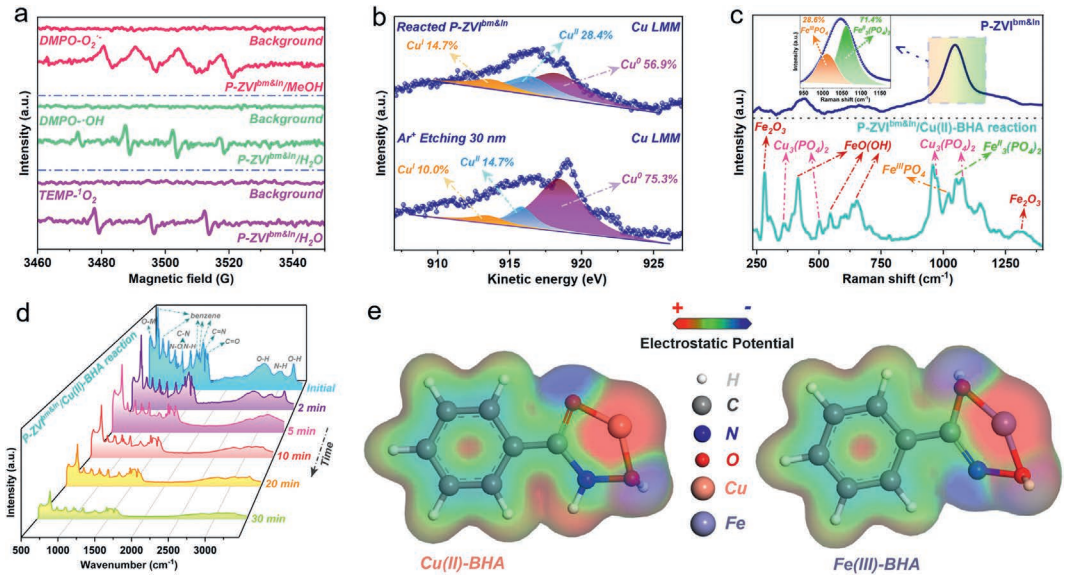


Fig. 3. (a) The EPR signals for DMPO-$O_2^{\bullet-}$, DMPO-$^{\bullet}$OH, and TEMP-$^1O_2$ within the P-ZVI$^{bm\&ln}$ system. (b) HR-XPS (Cu LMM) exploration of P-ZVI$^{bm\&ln}$ after Cu(II)-BHA decontamination. (c) Raman spectroscopy of P-ZVI$^{bm\&ln}$ and *in-situ* detection of Cu(II)-BHA removal. (d) *In-situ* ATR-FTIR spectroscopy for the P-ZVI$^{bm\&ln}$/Cu(II)-BHA reaction. (e) Electrostatic potential analysis of Cu(II)-BHA and Fe(III)-BHA.

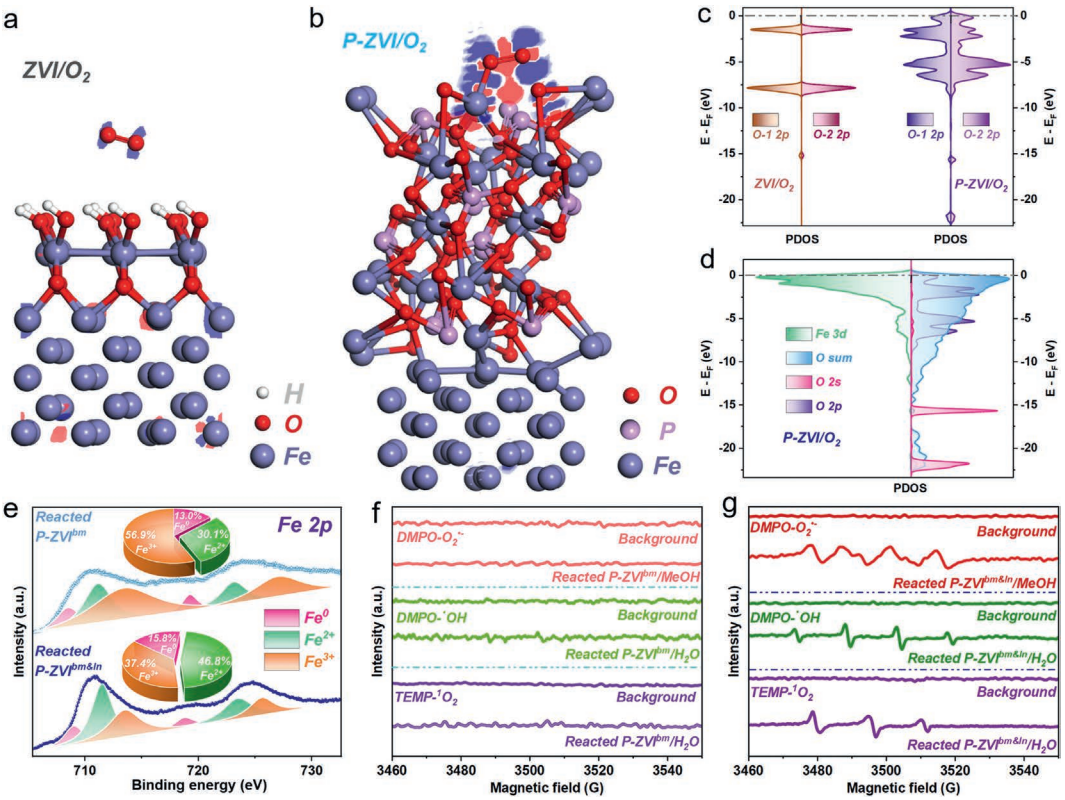


Fig. 4. The charge density difference for ZVI/O_2 (a) and P-ZVI/O_2 (b). Blue and red represent electron accumulation and depletion, respectively. (c) Project density of states (PDOS) investigation of O 2p in ZVI/O_2 and P-ZVI/O_2 systems. (d) PDOS investigation of total oxygen, O 2s, O 2p, and Fe 3d in P-ZVI/O_2 systems. HR-XPS (Fe 2p) analysis (e), and EPR examination of P-ZVI^{bm} (f) and P-$ZVI^{bm\&ln}$ (g) after Cu(II)-BHA removal.

ucts of Fe_2O_3 and FeO(OH) appeared; $Cu_3(PO_4)_2$ signals confirmed Cu^{2+} recovery *via* PO_4^{3-} precipitation (Fig. 3c) [25]. These results evidenced synchronous Cu recovery during P-$ZVI^{bm\&ln}$-mediated Cu(II)-BHA degradation.

In-situ ATR-FTIR monitoring of P-$ZVI^{bm\&ln}$-mediated Cu(II)-BHA removal revealed the gradual transformation of C=O (from Cu(II)-BHA) to C=N (from Fe(III)-BHA) signals, accompanied by an attenuation in BHA signals, suggesting replacement decomplexation and organic-ligands oxidative degradation (Fig. 3d) [26,27]. Therefore, BHA mineralization in the P-$ZVI^{bm\&ln}$/Cu(II)-BHA decontamination process was fundamentally driven by the oxidative degradation of Cu(II)-BHA and Fe(III)-BHA. The more negative zeta potential of P-$ZVI^{bm\&ln}$, compared to ZVI^{bm} and P-ZVI^{bm}, made it favorable for adsorbing the cationic Cu(II)-BHA and Fe(III)-BHA complexes *via* electrostatic attraction, thus promoting subsequent oxidative degradation (Figs. S27 and S28 in Supporting information). DFT calculations (frontier orbitals, electrostatic potentials, and Fukui functions) collectively confirm that the carbonyl and hydroxyl groups in Cu(II)-BHA, and the oxime and hydroxyl groups in Fe(III)-BHA, are prone to oxidative attack (Fig. 3e, Figs. S29 and S30 in Supporting information) [6]. Compared to Cu(II)-BHA, Fe(III)-BHA exhibited a higher HOMO and a lower $E_{(LUMO-HOMO)}$, suggesting a greater oxidative degradation propensity (Fig. S31 in Supporting information). LC-MS identified intermediates during the P-$ZVI^{bm\&ln}$/Cu(II)-BHA reaction (Fig. S32 in Supporting information). Based on these results, we proposed the degradation pathway of the complexed-metal (Fig. S33 in Supporting information). Replacement decomplexation of Cu(II)-BHA by Fe^{3+} generated Fe(III)-BHA, which was then degraded *via* Fe(III)-butenedioic acid complex. Part of Cu(II)-BHA could be degraded *via* oxidative decomplexation, as confirmed by the intermediate of Cu(II)-2-[(hydroxyamino)carbonyl]propanedioic acid complex. Acetic acid and pyruvic acid signals verified the profound oxidation and degradation of BHA. The theoretical prediction of bicarbonate as a primary carbonate species (pH 4.6-6.2) (Fig. S34 in Supporting information), coupled with its direct detection by LC-MS (Fig. S32), collectively confirms the mineralization of BHA.

In the $ZVI^{bm\&ln}$/Cu(II)-BHA system, adding ferrous or phosphate species slightly improved BHA degradation efficiency (Fig. S35 in Supporting information), indicating that the generation of ROS for degradation relied on the $\equiv Fe^{2+}$ sites formed after ZVI phosphorylation. Tafel analysis showed P-ZVI^{bm} had a lower corrosion potential and higher current than ZVI^{bm}; Liquid-nitrogen-quenching slightly lowered the corrosion potential of P-$ZVI^{bm\&ln}$ and increased its current. Electrochemical impedance spectroscopy (EIS) results indicated that the Nyquist half-radius of P-ZVI^{bm} was significantly smaller than that of ZVI^{bm}, while the radii of P-ZVI^{bm} and P-$ZVI^{bm\&ln}$ were close in value (Fig. S36 in Supporting information). DFT analysis of frontier orbitals showed that P-ZVI had elevated HOMO and decreased $E_{(LUMO-HOMO)}$, indicating enhanced electron transfer and migration due to phosphorylation (Fig. S37 in Supporting information). Molecular oxygen activation was contingent upon oxygen adsorption. DFT calculations elucidated that P-ZVI exhibited an oxygen adsorption energy of -0.79 eV, markedly lower than that of ZVI (0.17 eV), indicating phosphorylation facilitated oxygen adsorption (Fig. S38 in Supporting information). The charge density difference in ZVI/O_2 and P-ZVI/O_2 systems revealed significant electron transfer from P-ZVI to O_2, promoting O_2 activation to ROS (Figs. 4a and b). The weakened O_2 PDOS symmetry and marked Fe 3d-O 2p overlap in P-ZVI/O_2 indicated O_2 polarization and strong interactions (Figs. 4c and d) [28]. Population analysis showed lower O_2 Mulliken and Hirshfeld charges in P-ZVI than in ZVI, indicating higher electron accumulation and amplified O_2 activation potential. Bond length analysis further revealed

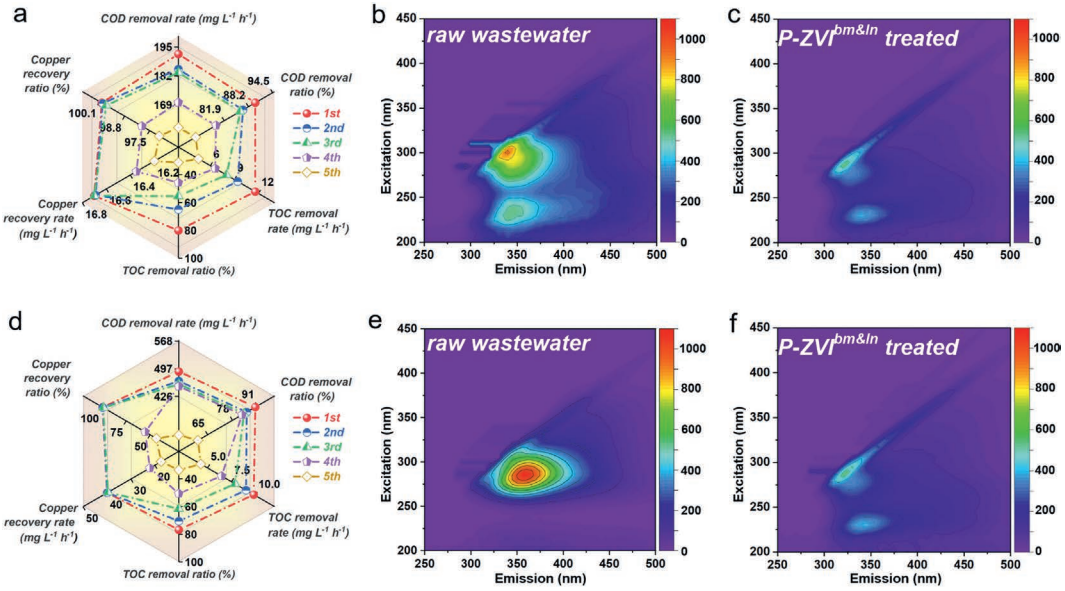


Fig. 5. Treatment results of copper mine wastewater from southeast (a) and southwest (d) China using P-ZVI$^{bm\&ln}$. The COD and copper ions in southeast and southwest mine wastewater were (~213.2/545.2 mg/L) and (~16.9/40.1 mg/L), respectively. Three-dimensional fluorescence spectra of raw and P-ZVI$^{bm\&ln}$ treated copper mine wastewater from southeast (b, c) and southwest (e, f) China.

a longer O-O bond in P-ZVI (1.48 Å) than in ZVI (1.24 Å), suggesting increased electron filling in the antibonding π^*2p orbital, leading to $O_2^{\bullet-}$ or O_2^{2-} formation [29]. Thus, phosphorylation boosted $\equiv Fe^{2+}$ sites and promoted O_2 adsorption/electron transfer, improving O_2 activation and ROS-mediated organic-ligand degradation by P-ZVI^{bm} and P-ZVI$^{bm\&ln}$.

Liquid-nitrogen-quenching caused surface cracks in P-ZVI$^{bm\&ln}$, exposing more internal Fe^0, which not only enhanced heavy-metal recovery but also reacted readily with leached Fe^{3+} (comproportionation: $Fe^0 + 2Fe^{3+} \rightarrow 3Fe^{2+}$), thus regenerating $\equiv Fe^{2+}$. The continuous efficacy of the heterogeneous Fenton-like reaction hinges on $\equiv Fe^{2+}$ regeneration, expectedly rendering P-ZVI$^{bm\&ln}$ more effective than P-ZVI^{bm} in the cyclic decontamination of Cu(II)-BHA by facilitating $\equiv Fe^{2+}$ regeneration. Post-reaction HR-XPS (Fe 2p) analysis, showed higher ferrous content (46.8 %) in P-ZVI$^{bm\&ln}$ than in P-ZVI^{bm} (30.1 %), emphasizing the vital role of ferrous regeneration in boosting the cyclic reactivity of P-ZVI$^{bm\&ln}$ in Cu(II)-BHA removal (Fig. 4e). EPR experiments performed on post-reaction P-ZVI^{bm} and P-ZVI$^{bm\&ln}$ showed that reacted P-ZVI$^{bm\&ln}$ exhibited distinctively superior ability to generate $O_2^{\bullet-}$, $^{\bullet}OH$, and $^1O_2$ compared to reacted P-ZVI^{bm} (Figs. 4f and g). Briefly, comproportionation-driven $\equiv Fe^{2+}$ regeneration in P-ZVI$^{bm\&ln}$ sustainably activates molecular oxygen, enabling continuous ROS generation for oxidative degradation.

Actual copper mine wastewater was collected from southeastern and southwestern China and treated by P-ZVI$^{bm\&ln}$. High concentrations of organic pollutants and heavy metals in actual mine wastewater led to low initial dissolved oxygen levels (<4.4 mg/L). P-ZVI$^{bm\&ln}$ efficiently treated residual organic agents and heavy metals through dissolved oxygen activation in the first two cycles (Fig. S39 in Supporting information), yet dissolved oxygen dropped to ~0.4 mg/L after two cycles, rendering activation relying solely on dissolved oxygen unfeasible. Hence, 5 mmol/L H_2O_2 was added, and Fenton reaction performance was evaluated. In the continuous treatment of southeastern mine wastewater, COD and TOC were efficiently removed, and Cu was recovered; residual COD and Cu met the discharge standards in 5 cycles (Fig. 5a). For southwestern mine wastewater treatments, residual COD met the discharge standards in 4 cycles, and residual Cu met the standards in 3 cycles (Fig. 5d). Three-dimensional fluorescence spectra analysis showed a notable attenuation of organics in copper mine wastewater from both sites (Figs. 5b and e) after P-ZVI$^{bm\&ln}$ treatment (Figs. 5c and f), consistent with COD and TOC removal. The treated wastewater complied with the requirements of GB 5084-2021 (COD $\leq$ 150 mg/L, Cu $\leq$ 0.5 mg/L), and seed germination assays confirmed ecotoxicity abatement after remediation (Fig. S40 in Supporting information), indicating favorable ecological safety. The reacted P-ZVI$^{bm\&ln}$ was reused as an iron-copper bimetal to decontaminate toxic DDTC, EX, and phenol. The removal ratios exceeded 99.4 %, 99.3 %, and 91.0 % in 5 cycles (Fig. S41 in Supporting information), and the leached copper concentrations all met the discharge standards (Fig. S42 in Supporting information), thus realizing the sustainable goal of metal recovery and "treating waste with waste".

In summary, this work developed a fissured-phosphorylated microscale zero-valent iron (P-ZVI$^{bm\&ln}$) for efficient one-step decontamination of Cu(II)-BHA complexes. The ferrous phosphate shell provided abundant $\equiv Fe^{2+}$ sites to activate molecular oxygen for generating ROS and oxidative degradation, while liquid–nitrogen–induced cracks exposed more Fe^0 cores to drive comproportionation ($Fe^0 + 2Fe^{3+} \rightarrow 3Fe^{2+}$), enabling sustained Fe^{2+} regeneration and ROS generation. This synergy achieved nearly complete copper recovery and BHA degradation without external oxidants or precipitants, offering a promising strategy for treating heavy–metal complex wastewater.

Declaration of competing interest

The authors declare that they have no known competing financial interests or personal relationships that could have appeared to influence the work reported in this paper.

CRediT authorship contribution statement

Yuhang Zhang: Writing – original draft, Visualization, Methodology, Investigation, Formal analysis, Data curation. **Haiming Cai:** Writing – review & editing. **Chuling Guo:** Project administration. **Guining Lu:** Supervision. **Zhi Dang:** Supervision, Project administration, Funding acquisition. **Xiao Liu:** Supervision. **Falong Jia:**

Writing – review & editing, Supervision, Project administration, Funding acquisition. **Zhihui Ai:** Supervision. **Chunhua Feng:** Writing – review & editing, Supervision, Project administration.

Acknowledgments

This work was financially supported by the National Key Research and Development Program of China (No. 2023YFC3207300), the Guangdong Natural Science Foundation (No. 2024A1515010861), the Local Innovation and Entrepreneurship Team Project of Guangdong Special Support Program (No. 2019BT02L218), and the National Natural Science Foundation of China (Nos. 22176068, 22276068).

Supplementary materials

Supplementary material associated with this article can be found, in the online version, at doi:10.1016/j.cclet.2025.112353.

References

[1] M.K. Li, J.Y. Wang, H.R. Shen, et al., Chem. Eng. J. 461 (2023) 142008.
[2] M.Q. Li, N. Chen, H. Shang, et al., Technol, Environ. Sci. 56 (2022) 10945–10953.
[3] Y. Luo, H. Li, H.L. Yang, et al., Environ. Sci-Nano 5 (2024) 2091.
[4] J.N. Zu, N.Q. Zhang, X.P. Liu, et al., Angew. Chem. Int. Ed. 64 (2025) e202415051.
[5] J. Wang, J.Y. Cai, X.Q. Zhou, et al., Sep. Purif. Technol. 354 (2025) 128945.
[6] H.Y. Zhou, J.L. Peng, X.G. Duan, et al., Environ. Sci. Technol. 57 (2023) 3334–3344.
[7] Y.H. Zhang, H. Zhang, N.Q. Zhang, et al., Sep. Purif. Technol. 354 (2025) 128772.
[8] Z.S. Wang, L.J. Qiu, Y.H. Huang, et al., Chin. Chem. Lett. 35 (2024) 109195.
[9] X.Y. Zou, Y.H. Zhang, K. Wei, et al., J. Hazard. Mater. 446 (2023) 130752.
[10] C. Piña, H. Arriola, N. Nava, J. Phys.: Conf. Ser. 217 (2010) 012037.
[11] E. Mattievich, J.A. Danon, J. Phys. Colloq. 37 (1976) 483–487.
[12] Y. Lv, L.T. Han, J. Shen, et al., Sep. Purif. Technol. 329 (2024) 125045.
[13] M.Q. Li, Y. Mu, H. Shang, et al., Appl. Catal. B: Environ. 263 (2020) 118364.
[14] Z. Yang, X.W. Ma, C. Shan, et al., J. Hazard. Mater. 368 (2019) 698–704.
[15] B. Özkaya, J. Hazard. Mater. 129 (2006) 158–163.
[16] S. Lata, P.K. Singh, S.R. Samadder, Int. J. Environ. Sci. Technol. 12 (2015) 1461–1478.
[17] S.H. Kow, M.R. Fahmi, C.Z.A. Abidin, S.A. Ong, N. Ibrahim, Desalin. Water Treat. 57 (2016) 29137–29142.
[18] Y.H. Zhang, D.L. Li, L. She, et al., J. Hazard. Mater. 465 (2024) 133009.
[19] M.F. Luo, H. Zhang, J. Zhao, et al., ACS ES&T Engg. 3 (2023) 64–72.
[20] W.X. Zheng, X. Luo, H.Y. Fu, et al., Environ. Sci. Technol. 58 (27) (2024) 12212–12224.
[21] E.-T. Yun, J.H. Lee, J. Kim, H.-D. Park, J. Lee, Environ. Sci. Technol. 52 (2018) 7032–7042.
[22] W.S. Li, Z.Q. Sun, Y.D. Chen, et al., Chin. Chem. Lett. 37 (2026) 111791.
[23] X. Zhang, H.W. Sun, Y.B. Shi, et al., Water Res. 235 (2023) 119828.
[24] M.Z. Liao, S.X. Zhao, K. Wei, H.W. Sun, L.Z. Zhang, Appl. Catal. B: Environ. 330 (2023) 122619.
[25] J. Koo, B.S. Bae, H.K. Na, J. Non-Cryst. Solids 212 (1997) 173–179.
[26] M.A. Ibrahim, A.M. Nada, D.E. Kamal, Indian J. Pure Appl. Phys. 43 (2005) 911–917.
[27] Z. Wei, Y.H. Hu, H.S. Han, W. Sun, J. Colloid Interface Sci. 562 (2020) 342–351.
[28] Y.M. Wei, P. Song, Y. Wen, et al., Water Res. 268 (2025) 122656.
[29] Z.P. Yang, Y.B. Shi, H. Li, et al., Environ. Sci. Technol. 56 (2022) 3587–3595.